

PAPER • OPEN ACCESS

## A soft piezoelectric elastomer with enhanced piezoelastic response

To cite this article: Lorenzo Nicolini *et al* 2023 *Smart Mater. Struct.* **32** 105003

View the [article online](#) for updates and enhancements.

### You may also like

- [SH guided wave excitation by an apparent face-shear mode \( \$d\_{36}\$ \) piezocomposite transducer: experiments and theory](#)  
Hongchen Miao, Lei Xu and Hao Zhang
- [An experimental investigation of piezoelectric P\(VDF-TrFE\) thick film on flexible substrate as energy harvester](#)  
Chow Khoon Keat, Kok Swee Leong and Lau Kok Tee
- [A review of piezoelectric polymers as functional materials for electromechanical transducers](#)  
Khaled S Ramadan, D Sameoto and S Evoy

# A soft piezoelectric elastomer with enhanced piezoelastic response

Lorenzo Nicolini\* , Andrea Sorrentino  and Davide Castagnetti 

University of Modena and Reggio Emilia—Department of Sciences and Methods for Engineering,  
Via G. Amendola 2, 42122 Reggio Emilia, Italy

E-mail: [217058@studenti.unimore.it](mailto:217058@studenti.unimore.it)

Received 14 March 2023, revised 21 July 2023

Accepted for publication 10 August 2023

Published 24 August 2023



## Abstract

This work aims to study, develop, and validate a soft piezo-polymer with enhanced piezo-elastic response and easy castable in a free shape through a single and easy process. The work identified a novel formulation for soft piezopolymers based on ambient temperature polymerizable silicone rubber, easily fabricable in 3D printed plastic moulds. Combining polymerizable silicone with a barium titanate ( $\text{BaTiO}_3$ ) ceramic powder and defining a detailed fabrication procedure of casting, curing and high voltage poling, we defined how to obtain a promising soft piezoelectric elastomer for countless sensing applications. This study includes information about the mould design used to realize, cure and polarize cylindric elastomeric specimens. This piezopolymer stands out for its flexibility, softness, easy fabrication at ambient temperature and obtainability in multiple shapes and bulky 3D geometries. Finally, we investigated different configurations of the piezopolymer formulation analysing the powder concentration and voltage polarization effects over the mechanical, piezoelectric and morphological characteristics. The specimens exhibit a high induced polarization  $d_{33}$  with values up to  $22.5 \text{ pC N}^{-1}$ , comparable with poled  $\beta$ -phase polyvinylidene difluoride. We finally underlined limits encountered in the most extreme configurations.

Keywords: silicone, soft piezopolymer, polarization, polymerization, optimization, electrostatics

(Some figures may appear in colour only in the online journal)

## 1. Introduction

This work features on the development and validation of a novel soft piezo-polymer enhanced with piezoelectric properties, and easy castable in free shapes.

Piezoelectric materials are largely used for sensing or energy harvesting as a simple and reliable solution in several applications, from piezoelectric accelerometers or force sensors [1–4], vibration energy harvesters [5–13], to actuators

[14, 15]. Some of them have found peculiar complex and elaborated methods to use standard zirconate titanate (PZT) plates as actuators [16, 17]. Most applications rely on piezoceramic materials, but also piezoelectric polymers are of interest for applications which need a mechanically flexible material, such as tactile sensing and acoustic devices [1, 2, 18–24]. Besides that, also commercial MFCs (macro fibre composites) are often used in robotic and especially soft robotic applications as actuators exploiting their flexibility [25, 26].

Actual piezoceramic materials are stiff, brittle, expensive, available only in standard shapes and with low thicknesses [27]. Moreover, different classes of natural piezopolymers exists (bulk piezoelectric, piezoelectric polymer composite, voided charged polymers, polyvinylidene difluoride (PVDF)), but with very low piezoelectric response [18, 28] compared to classical piezoceramic. Their flexibility makes them

\* Author to whom any correspondence should be addressed.



Original content from this work may be used under the terms of the [Creative Commons Attribution 4.0 licence](https://creativecommons.org/licenses/by/4.0/). Any further distribution of this work must maintain attribution to the author(s) and the title of the work, journal citation and DOI.

suitable in multiple other applications where common brittle piezoceramics generally fail, but they settle extremely far from the desired softness and hyper elasticity required in many sectors. A straightforward solution to these limitations is to combine common commercial high performance piezoelectric devices, like MFC, with elastomers or elastomeric components creating composite soft piezoelectric devices [29, 30]. However, internal mechanical anisotropies limit the number of obtainable geometries that have to be carefully evaluated and designed each time. Moreover, difficult connections, high costs, fabrication times and efforts are triggering research to find out integrated solutions based on new materials.

Nowadays, the focus of this research is to investigate, develop and validate new piezopolymers with a strong piezoelectric response (close to piezoceramics) but possibly softer than traditional piezopolymers (such as PVDF). Many researches can be found in the literature focusing on the development of soft and flexible piezoelectric elastomers in many different configurations and shapes for a number of applications. In particular, Banno investigates a possible solution to obtain flexible piezo-wire elements [31] and reports different piezoelectric and dielectric properties of theoretical flexible composites of synthetic rubber and piezoelectric ceramic particles [32]. Hikita *et al* [33] compares the piezoelectric properties of the porous PZT with the porous PZT composite with silicone rubber. Qi *et al* [34] shows how to obtain stretchable and wearable piezoelectric materials using piezo-ribbons printed onto rubber. In the field of human body applications, Tsai *et al* [35] demonstrates the fabrication of piezoelectric rubber films for heartbeat sensing and human energy harvesting, while Wang *et al* [36] designs and microfabricates piezoelectric rubber bands for energy harvesting applications from breathing and limb motions. Again, Wang *et al* [37] shows the microfabrication of piezoelectric rubber films for highly sensitive impact measurements. Many other solutions focus on piezoelectric low thickness elastomers with different fabrication processes and final purposes, but involving ad-hoc geometries or thin surfaces elastomeric devices [38–46].

Mamada *et al* [47] reports the realization of a piezoelectric thermosetting rubber based on PZT powder through a casting process and has investigated its piezoelectric response. This represents a revolutionary method to create free shape thermosetting piezopolymers usable in a large field of applications, but the process requires high temperatures to thermoset rubber and a peculiar equipment.

On the same line Fu *et al* [48] develops unpolarized soft and 3D free shape piezoelectric soft elastomers based on crosslinked polyacrylonitrile. This solution shows important achievements in term of voltage responses. However, it presents a very high drying shrink effect which can lead to distortions on the final casted element and requires a quite complex and expensive fabrication procedure.

Despite these researches investigate the development of flexible and soft piezopolymers, these materials are oriented to specific field of applications with fixed geometric properties [34–37]. Each solution has a precise application field, and it is focused on a peculiar issue in defined situations. Many

other solutions offer the possibility to obtain thin free shape surfaces. Among many researches, Mamada and Fu proposed methods to fabricate 3D free shape bulky soft piezoelectric elements, but through complex processes at non ambient temperature or with needs of further treatments.

To overcome these limitations, the present work focuses on the development of a new versatile piezoelectric material with the elastic properties of common silicone-based elastomers, castable in any desired shape through a simple ambient temperature process.

Specifically, the work identified a novel formulation and fabrication procedure for soft and bulky piezopolymers based on ambient temperature polymerizable silicone rubber, easily castable in 3D printed plastic reusable moulds.

We combined a liquid polymerizable silicone-based elastomer (Sylgard 184 Dow Chemical [49] with a BaTiO<sub>3</sub> (barium titanate [50])) 99% pure powder. In order to orient the piezoelectric crystals immersed in the solution, we performed high voltage polarization through the application of a high electric field simultaneously to the polymerization by catalyst. A specific tool was designed and 3D printed to cure the solution and overcome all the practical issues. The tool consists in a mould with a cylindrical cavity which contains the mixture during the curing process, giving the desired shape to the piezopolymer, and able to house two electrodes for the simultaneous polarization. Specimens' morphological characteristics are shown, presented and discussed.

To investigate the optimal formulation of the material, we performed an extensive test plan that considered the powder concentration, and the polarization voltage.

The material validation involved compression tests on cylindrical specimen to investigate the electromechanical response (output voltage, force, and displacement): this allowed to retrieve the engineering constants and the piezoelectric coefficients of the material. Experimental tests showed remarkable results in terms of output voltage signals, in addition to a low elastic modulus and high elastic strain response on the mechanical side.

This material is suitable for multiple and various applications such as condition monitoring, soft robotics, sensorized dampers, biomedical and wearable devices, sport equipment, human motion monitoring, impact sensorized protection and many other sensing applications. Even though the proposed thin sheet specimen is particularly indicated and designed for compression test specimens, it can constitute a sensing elastomeric piezoelectric shim.

## 2. Method

### 2.1. Materials

To develop the new piezoelectric polymer, we investigated a mixture of a piezoelectric powder and a silicon elastomer. The piezoelectric agent is a BaTiO<sub>3</sub> (barium titanate), 99% pure ceramic powder, with high piezoelectric properties, a formula weight of 233.19 g mol<sup>-1</sup>, and a nominal particle size lower than 3 μm [50]. The choice for BaTiO<sub>3</sub> has three main

reasons: it provides good performances among all piezoelectric powders, it is commercially available and the least expensive of other ceramic powders. According to the comparison reported in the work from Mamada *et al* [47], we chose this powder particle size since it provides higher performances, in terms of induced polarization per unitary stress ( $d_{33}$ ), than other piezoelectric powders of smaller diameter. This better performance can be imputed to the stronger effect of polarization on large diameter particles.

The selected elastomer is the bi-component Dow Chemical Sylgard 184 [49], which consists of a liquid silicone base and its own catalyst for the polymerization process. Two are the peculiar properties that make this elastomer an ideal candidate for developing a novel piezoelectric material. First, its high viscosity ( $3.5 \text{ Pa} \cdot \text{s}$ ) before curing, that prevents the high-density piezoelectric powder from settling on the bottom. Second, the high dielectric strength ( $21 \text{ kVmm}^{-1}$ ) that avoid breakdowns during polarization. Third, the low hardness (43 Shore A) of the cured silicone, and fourth, a remarkable ultimate tensile strength (6.7 MPa) if compared to other polymerizable silicones.

The process that leads to the piezoelectric polymer consists of three steps: mixing, moulding and degassing, polarization and curing.

## 2.2. Mould design

Figure 1 presents the schematic of the mould assembly, purposely designed to cast the specimens of the material: its peculiar structure allows to contain and polarize the mixture during curing and give the desired shape to the final sample. The main constraint in the mould design was given by the need for polarization of the material and the need to have a geometry suitable for compression tests. These reasons oriented our choice toward a circular disc, which ensures a uniform electric field, and limited the specimen thickness. Since the process occurs at low temperature and it is necessary to ensure high dielectric strengths, our tool consists in a plastic acrylonitrile butadiene styrene mould realized by filament fused fabrication 3D printing, using a Dimension BST 768 Stratasys [51]. The cylindrical mould has a radius of 37.5 mm ( $R$  in figure 1) and a height of 25 mm ( $h$  in figure 1). An internal cylindrical cavity defines the final shape of the samples: on top and bottom of it, the mould houses two circular hardened steel electrodes, which are connected to an external high voltage source for the polarization of the mixture. The upper ( $B$  in figure 1) and lower electrodes ( $C$  in figure 1) have a diameter respectively equal to 45 mm ( $d_1$  in figure 1), and 50 mm ( $d_2$  in figure 2). This set up works originating an electric field orthogonal to the bases of the cylindrical sample. A consistent gap from the ground is ensured to electrically insulate the system with the external environment. To facilitate degas the specimen from air bubbles during polymerization, the internal cavity has three radial inclined ducts acting as air exhausts ( $A$  in figure 1), angularly equispaced at  $120^\circ$ .

Through an electrostatic finite element analysis of the system during polarization, we chase the dimensions of the cast

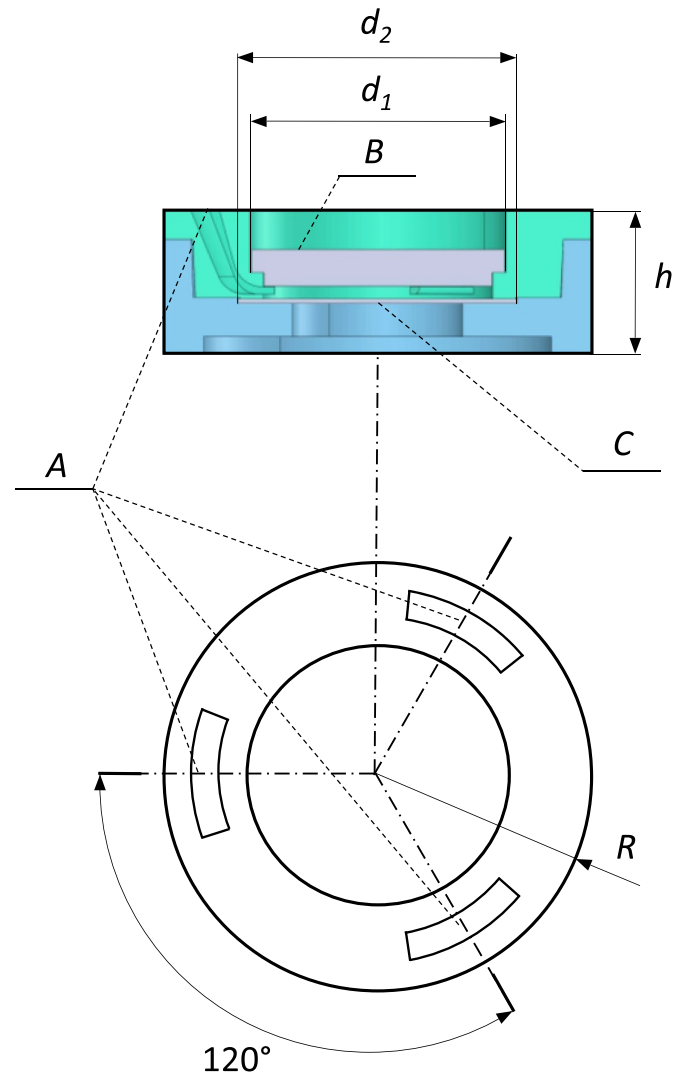


**Figure 1.** Schematic of the mould assembly: frontal (top) and section view (bottom). Maximum radial encumbrance ( $R$ ) and height ( $h$ ), respectively. Upper ( $B$ ) and lower ( $C$ ) steel electrodes with  $d_1$  and  $d_2$  as diameters, respectively. Air exhausts indicator ( $A$ ).

that ensure a nearly constant distribution of the electric field in the region of interest and avoid electric breakdowns between the steel electrodes detecting possible electric field concentration points.

This simulation was implemented through the software FEMM 4.2 (Finite Element Method Magnetics) with some assumptions and simplifications: first, the model is axisymmetric; second, the simulation describes a single air exhaust outlet ( $E$  in figure 2) which extends continuously on the entire circumference of the mould. This conservative simplification allows us to study the system as axisymmetric, remaining consistent with the main purpose of the simulation.

As figure 2 shows, the dominium of the simulation includes the two electrodes as conductors ( $A$  in figure 2), the plastic mould ( $C$  in figure 2), the silicone elastomer specimen ( $D$  in figure 2) and the surrounding air as dielectrics ( $B$  in figure 2), which is an external unlimited region. The dimensions of the

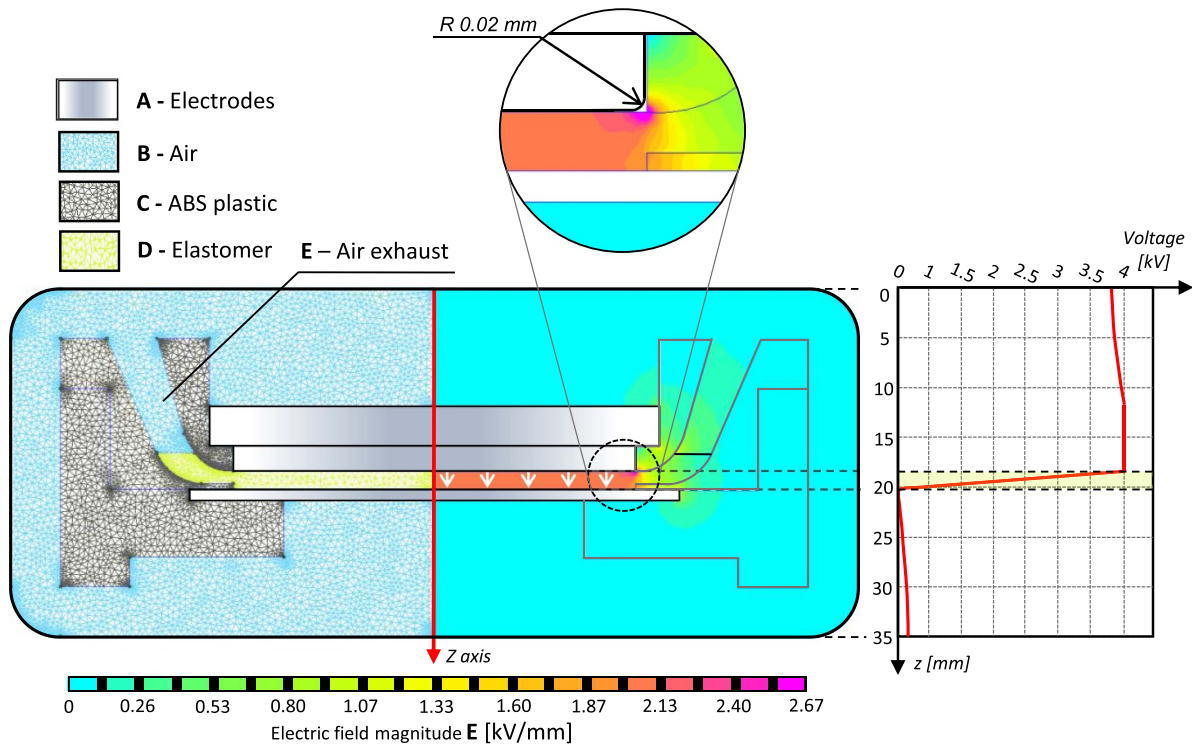


**Figure 2.** Electrostatic model: axisymmetric triangular mesh on the left hand, contour plot of the electric field magnitude on the right hand, and plot of electric potential prediction along the entire height of the system.

mould correspond to the geometry in figure 1. Axisymmetric triangular elements were used to discretize the model, using smaller elements near the boundaries, with exception of the two electrodes that are described as voltage sources. The model applies a relative electric potential  $V_0 = 0\text{V}$  on the lower electrode and  $V_{\text{high}} = 4\text{kV}$  on the upper electrode, which represents the maximum voltage level assumed for this work.

A fillet has been introduced in the lower edge of the upper electrode ( $R$  in figure 2) in order to correctly simulate the increase of the electric field due to the local electric charge concentration and to avoid a singularity in the model. The fillet has a radius of about  $0.02\text{ mm}$  which is consistent with the lathe machining process and tool used to obtain the upper electrode.

The contour plot in figure 2 shows that the electric field is nearly constant all over the volume occupied by the mixture: a local increase of electric field only occurs along the edge with fillet. The plot on the right shows the relative electric potential through the entire height of the mould calculated along the axisymmetric axis ( $Z$  axis) of the mould. The two electrodes impose the electric potential difference which behaves linearly in the elastomer region (yellow zone in the plot).

### 2.3. Procedure of fabrication

To obtain the specimens, the casting procedure consisted of three sequential steps.

- **Mixture preparation.** The piezoelectric powder was mixed to the silicone matrix through a mixer, inside a bowl, for

a time of 3 min. Once the powder has completely diffused into the liquid silicone, the catalyst was added to start the polymerization. After a second mixing lasting 1 min, the solution was casted into the mould.

- **Air evacuation.** Since mixing processes incorporates air into the liquid, it was necessary to remove bubbles avoiding internal cavities in the specimens. Thus, the whole mould was placed in a vacuum chamber that works with a Venturi valve, receiving the air flow from an air compressor. The vacuum relative pressure reached was  $-0.88\text{ bar}$ . To obtain the best results, the air evacuation process was repeated two times, 10 min long each. In the first step the top electrode was not applied, thus the mould was open on the top. Instead, in the second step the top electrode was set up, thus the cavity was completely closed, with exception of the degas ducts, which facilitate the exit of the trapped air (figure 1).

Once the specimens were degassed, they were simultaneously polarized and cured.

- **Polarization and curing.** We performed the polarization of the specimen by applying an electric potential to the electrodes. The electric potential comes from a series of two power supply: a first power supply (AIM-TTi CPX400A Dual 60 V/20 A [52]) converts power from the supply network (220 V, AC) to an output signal of 12VDC; this output voltage becomes inputs to a high voltage DC – DC converter (XP Power Emco high voltage corporation—CB101 [53]), which provides an output voltage up to 10kV.



A potentiometer applied to this second device allowed to continuously regulate the output voltage. Positive and negative output voltage cables from the high-tension converter were welded to the electrodes. Simultaneously, the silicone polymerization occurred at 25 °C with a relative humidity of 40% in a controlled ambient temperature through a climatic chamber for 30 h, a curing time that according to the silicon manufacturer ensures a complete curing process. The specimen was then extracted from the mould.

#### 2.4. Sample preparation and test plan

The specimens obtained from the casting procedure described in the previous Section show a good polarization effect in the majority of the volume except for the external edge and the lateral surface which usually present some imperfections. For these reasons, we extracted smaller cylinders from the casted specimen with a die cutting operation, excluding the external edge. From each cast we got three identical specimens with a diameter of 16.4 mm and a height around 2.5 mm.

The test plan investigated the effect of two variables each of them over three levels: powder concentration (25%, 50%, 65% by weight) and polarization voltage (0, 2 and 4 kV). We performed three replications for each configuration for a total of 27 specimens, and, by carefully observing the specimens through an optical Image Dimension Measurement System (Keyence IM-8030), we selected the best specimens. Specifically, we chose those without defects in the matrix and showing a uniform powder distribution. For each of the nine combinations of polarization voltage and powder concentration of the test plan, figure 3 presents a picture (1.5 scale factor) of the chosen specimens (front and side view): for each specimen we reported the electric capacitance in unloaded condition,  $C_0$ , measured through an inductance capacitance resistance (LCR) meter, and the Shore A hardness registered through a manual and portable hardness tester (Mitutoyo durometer [54]). The hardness values reported in figure 3 correspond to the average between the five measurements on the top face or bottom face, respectively. The measurements were performed on the centre of the face plus four points on a circumference: specifically, for each sample we reported the higher average value among the two.

Not polarized specimens, shown in the left column in figures 3(a), (d) and (g), appear very similar to each other despite of the different powder concentration: BaTiO<sub>3</sub> diffused in the silicone base creating opaque white specimens in all the three cases shown. This effect proves that despite of the higher density of the BaTiO<sub>3</sub> powder than the polymer matrix, the powder does not settle on the bottom during polymerization thanks to high silicone viscosity. The deposition effect is the proof that the polarization occurred. The internal electric field can be affected by the dipole's orientation. In any case the electric field seen by particles dipoles is exactly what we constantly applied externally.

On the other hand, in polarized specimens (second and third column in figure 3) clearly emerges a powder concentration on a side of the specimen, specifically for the low polarization voltage (2 kV, first row in figure 3). Since unpolarized

specimens exhibited a uniform distribution of the BaTiO<sub>3</sub> powder in the polymer matrix, as testified by the homogeneous opaque surface, the electric field applied during polarization must be the cause of separation of the mixture, in addition to particle orientation: the powder has been attracted on the left side keeping more transparent the right side. However, by increasing the BaTiO<sub>3</sub> concentration (second and third rows in figure 3), the large amount of powder in the mixture fills the whole volume of the specimen, and transparent region becomes negligible (50% concentration) or disappears.

The heterogeneity is present since there are two ingredients mixed. The anisotropy observed in powder distribution in the plane of the specimen highlights the fact that the process repeatability has margin to be improved thus improving the pure piezoelectric performances of the proposed material. Main improvements would consist in reducing the electrode surface roughness and increasing the precision of mechanical couplings.

Moreover, figure 4 illustrates a matrix that compares four specimens horizontally disposed with the same powder concentration (25%) at various polarization voltage level (figure 4(a) 0 kV, figure 4(b) 1 kV, figure 4(c) 2 kV and figure 4(d) 4 kV). Each column refers to a single sample and reports three acquisitions at different magnifications through a scanning electron microscope (SEM) in backscattering mode with a low vacuum condition of 100 Pa (absolute pressure). After cooling in liquid nitrogen each specimen has been broken obtaining a clean fracture surface of the elastomer: this allowed to observe the correspondent internal section. We framed the visible field of the SEM onto the separation boundaries encountered in all the specimens except for the unpolarized one. From the first row of the polarized samples, it appears that while the white side remains approximately constant in colour and thickness, the transparent side becomes hazier as the polarization voltage increases. This can be imputed to the higher electric field that induces particles to a self-alignment along the electric field lines increasing the amount of powder particles in the transparent side. Moreover, the unpolarized specimen shows a very balanced particles diffusion with no interactions among them in figure 4(a). On the other side, polarized specimens depict a strong separation boundary in figures 4(b)–(d). As the voltage increases, it is easy to see that more free particles float in the transparent side, which causes the macroscopic haze effect, whereas particles connections and agglomerates are more likely in the white side. In particular, the 4 kV specimen reveals vertical straight-line patterns due to the polarizing electric field. The last row illustrates BaTiO<sub>3</sub> particles from the closest point of view highlighting their average size of 1 μm.

### 3. Experimental assessment

#### 3.1. Test bench

The experimental assessment aimed to perform electromechanical characterization of the piezoelectric polymer through compression tests.

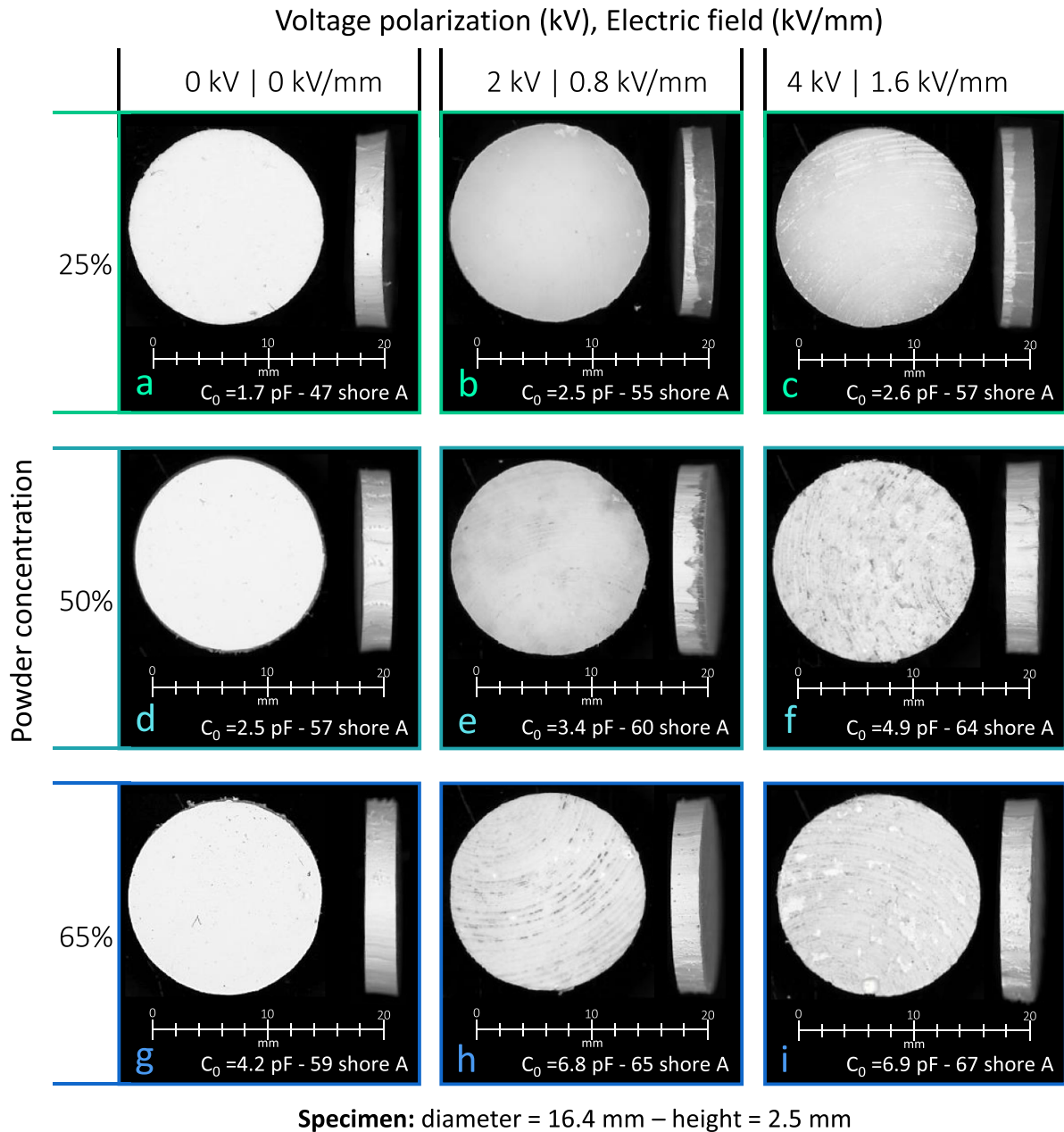


**Figure 3.** Overall view of the specimens' configurations investigated: each of the three columns correspond to a level of polarization voltage (0, 2, 4 kV); each of the three rows report a level of powder concentration (25%, 50%, 65%). For each configuration the sample capacitance in unloaded conditions ( $C_0$ ) and the Shore A hardness (average of the values measured on the harder face).

The test bench included an electromechanical testing machine, Galdabini Sun 500 [55], with a load capacity of 5 kN, controlled by a proprietary software installed on a PC, and an acquisition board, National Instruments I/O USB-6251 device [56] connected to a notebook. Figure 5(c) shows a picture of the testbench set-up.

### 3.2. Test procedure

The tests investigated two strain levels,  $\varepsilon_m$ , equal to 25% and 40% of the specimen thickness. The compression tests involved two consecutive steps. First, a quasi-static linear ramp that compresses the specimen up to half of the total

desired strain ( $\varepsilon_m/2$ ), with a speed of  $1 \text{ mm min}^{-1}$ . Second, starting from the previous deformation, a cyclic compression with a sine displacement law having an amplitude equal to  $\varepsilon_m/2$  and a frequency of 0.5 Hz. This last step applies a cyclic compression on the specimen from zero up to  $\varepsilon_m$  of its thickness.

Two thin steel plates were applied to the specimen, respectively on top and bottom faces: these plates were electrically insulated by a thin and transparent PVC film to prevent interactions with the test machine. Two circular conductor laminae were applied on the two faces of the specimen (see section 'acquisition voltage circuit') and electrically connected to the data acquisition board, with a resistive load connected in

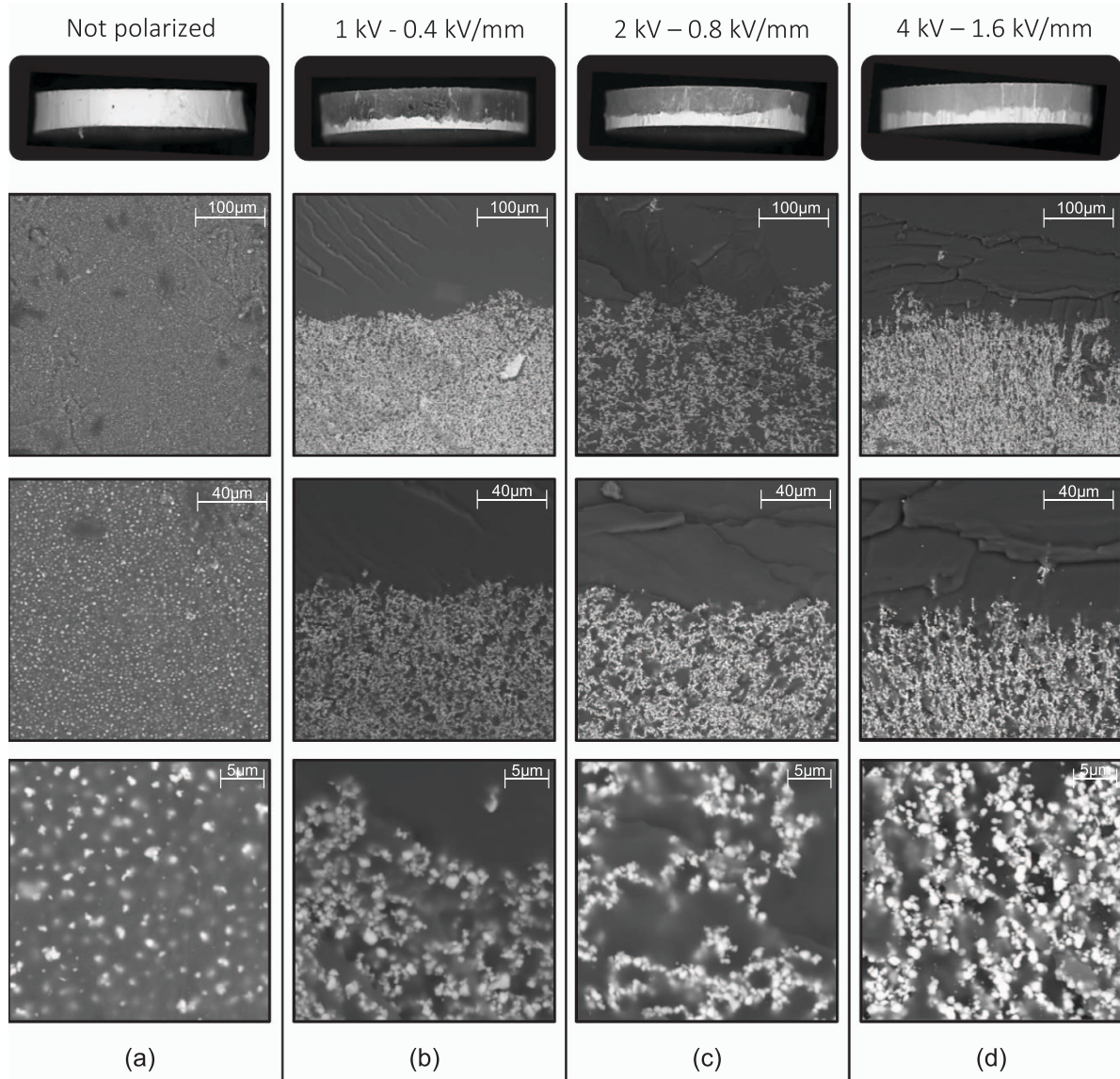


**Figure 4.** In the first row, pictures of four types of configurations investigated, showing the haze effect at different levels of polarization (figure (a) 0 kV, (b) 1 kV, (c) 2 kV and (d) 4 kV); from row two to four, scanning electron microscope acquisitions in backscattering mode at different magnifications (white BaTiO<sub>3</sub> particles immersed in the dark grey silicone matrix).

parallel. Acquired voltage output data were sent and stored by an external PC.

### 3.3. Acquisition voltage circuit

Figure 5(a) shows the physical connection we implemented. To stabilize the output voltage signal ( $V_{out}$ ) measured by the acquisition board we applied a resistive load  $R_L$  of 70 M $\Omega$  in parallel with the piezopolymer (shown in figure 5(a)).

To calculate the corresponding open circuit output voltage removing both the effect of the applied resistance  $R_L$  and the effect of the excitation frequency, we implemented an analytical model based on the equivalent circuit proposed by Park [57] for a piezoelectric material (figure 5(b)): the circuit also included the additional resistive load  $R_L$ .

Equation (1) defines the ratio between the output voltage  $V_{out}$  and the input voltage  $V_{in}$  of the circuit in figure 5(b),

$$\frac{V_{out}(t)}{V_{in}(t)} = \frac{V_o \cdot e^{i(\omega t + \xi)}}{V_i \cdot e^{i\omega t}} = \frac{\omega^2 C^2(\varepsilon) R_L^2 (R(\omega) + R_L) + i\omega C(\varepsilon) R_L}{\omega^2 C^2(\varepsilon) (R(\omega) + R_L)^2 + 1} \quad (1)$$

where  $\omega$  is the pulsation of excitation,  $R_L$  is the resistive load,  $C(\varepsilon)$  is the electric capacitance which varies as a function of the axial strain of the specimen  $\varepsilon$ ,  $V_o$  and  $V_i$  are respectively the amplitude of  $V_{out}(t)$  and  $V_{in}(t)$ ,  $\xi$  is the phase between  $V_{out}(t)$  and  $V_{in}(t)$ , while  $R(\omega)$  represents the piezoelectric internal resistance that varies over the excitation frequency. From equation (1), we obtained module and phase of the voltage ratio, shown in equations (2) and (3), respectively,



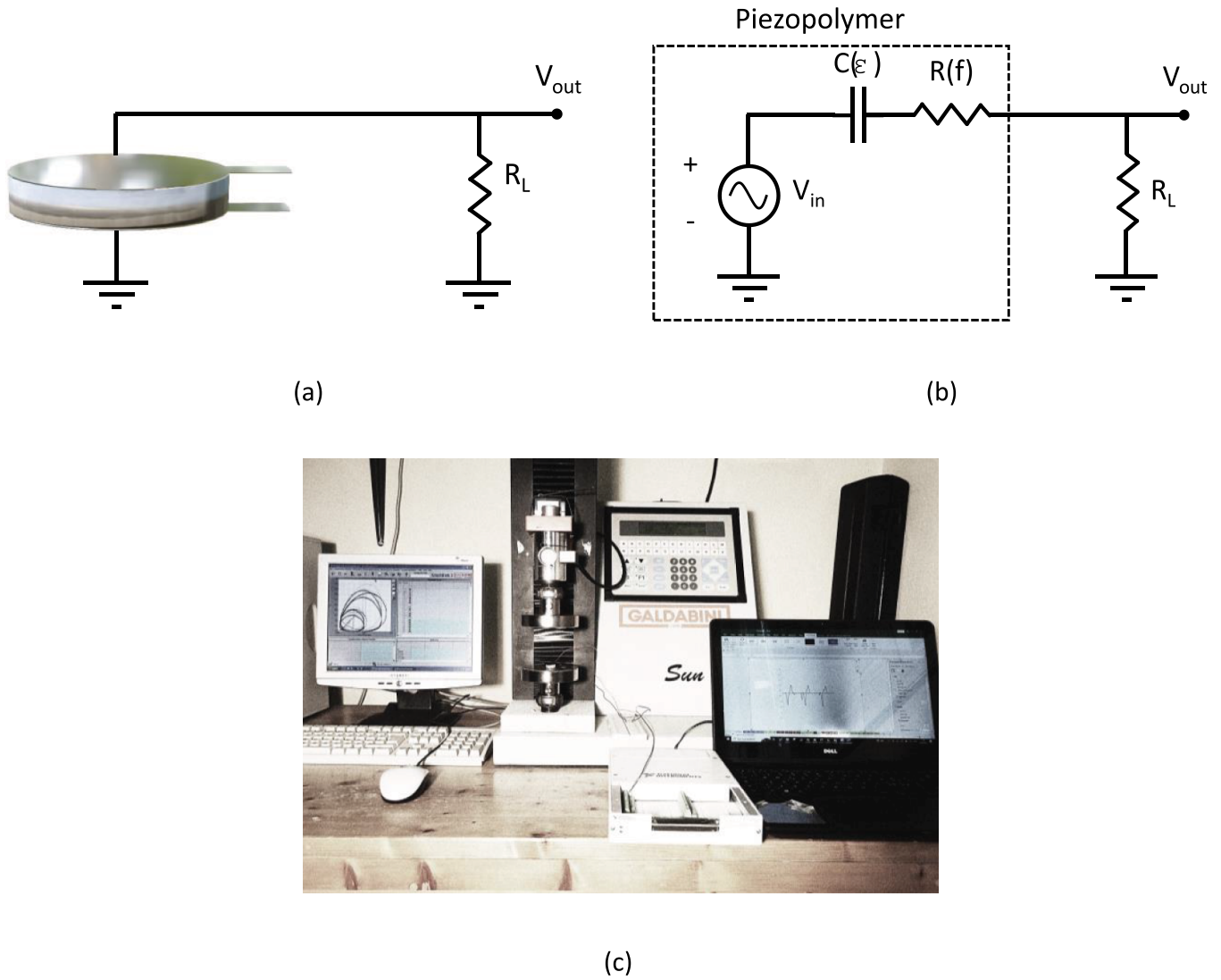


Figure 5. Sketch of the acquisition voltage circuit: (a) real connection, (b) equivalent circuit, (c) picture of testbench setup.

$$\frac{V_o}{V_i} = \frac{\omega C^2(\varepsilon) R_L}{\sqrt{\omega^2 C^2(\varepsilon) (R(\omega) + R_L)^2 + 1}} \quad (2)$$

$$\xi = \arctan\left(\frac{1}{\omega C(\varepsilon) (R(\omega) + R_L)}\right). \quad (3)$$

Focusing on the module, it is easy to obtain the voltage input  $V_i$  removing the dependency of the circuit characteristics and excitation frequency.

### 3.4. Piezoelectric coefficient

Considering the chosen shape and dimensions of the chosen specimens, we tested the samples in the polarization direction only, and thus calculated the  $d_{33}$  piezoelectric coefficient (i.e. mechanical compression directed in the same direction of poling). To obtain the piezoelectric coefficient  $d_{33}$  for the proposed piezopolymer, we need the piezopolymer capacitance in loaded conditions.

By relying on the work from Al Ahmad and Allataifeh [58], starting from the measured values of the unloaded capacitance  $C_o$  (see figure 3), we calculated the value of the loaded capacitance  $C(\varepsilon_m)$ , by exploiting the following equation:

$$C(\varepsilon_m) = \frac{C_o}{d(1 - \varepsilon_m)^2} \quad (4)$$

where  $d$  is the specimen thickness in unloaded condition and  $\varepsilon_m$  is the applied strain, previously specified. This equation assumes the incompressibility of the material (i.e. Poisson's ratio  $\nu = 0.5$ ), which leads to a neglectable simplification.

Thus, the piezoelectric coefficient  $d_{33}$  can be obtained as described by the equation (3),

$$d_{33} = \frac{Q}{F} = \frac{C(\varepsilon_m) V_i}{F} \quad (5)$$

where  $Q$  is the electric charge and  $F$  is the compression force.

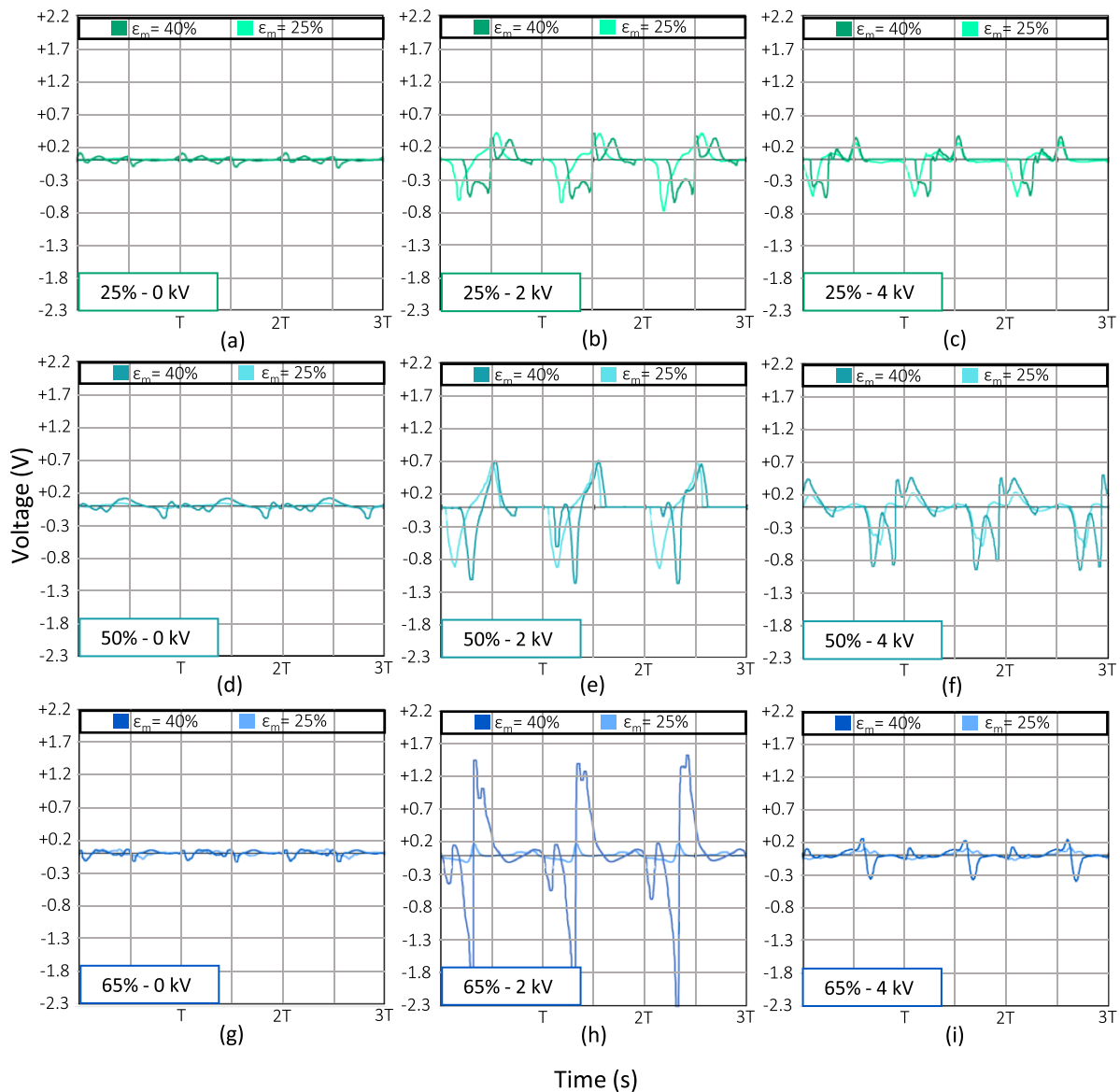


**Figure 6.** Plot of the output voltage signals: first, second, and third row refer to 25%, 50%, and 65% of ceramic powder concentration, respectively. Left, middle, and right column refer to 0, 2 and 4 kV polarization voltage, respectively. The letter at the bottom of each plot refers to the correspondent configuration.

#### 4. Results and discussion

For each of the specimens identified in figures 3 and 6 reports three periods of the voltage signal registered in the electromechanical tests described in section 3. Each plot refers to a single configuration, and shows two curves, corresponding to different levels of the maximum strain ( $\epsilon_m = 25\%$ ,  $\epsilon_m = 40\%$ ). The left, middle and right column refer, respectively, to 0, 2 and 4 kV polarization voltage, while the first, second, and third row refer, respectively, to 25%, 50% and 65% powder concentration by weight.

Voltage signals are well defined in all the plots shown, and figure 6 highlights different interacting effects. By comparing the left, middle and right column we can observe the effect of polarization voltage: the left column in figure 6

(non-polarized specimens) shows a very low output voltage compared to the others, thus proving that polarization is needed to obtain piezoelectric properties. The middle one (2 kV polarization) shows the higher output voltage for all the powder concentration levels, while the configurations in the right column (4 kV polarization) exhibit values close to but lower than 2 kV polarized specimens, with the exception of the configuration in figure 6(i), showing a clearly low performance. By focusing on the two curves in each plot, we can see that the output voltage for a strain  $\epsilon_m = 40\%$  is generally stronger than the signal registered at  $\epsilon_m = 25\%$  and the amplitude of the output voltage is strongly non-linear with the applied strain.

With regard to the lower output voltage registered for the 4 kV polarized configurations (figures 6(c), (f) and (i)), two

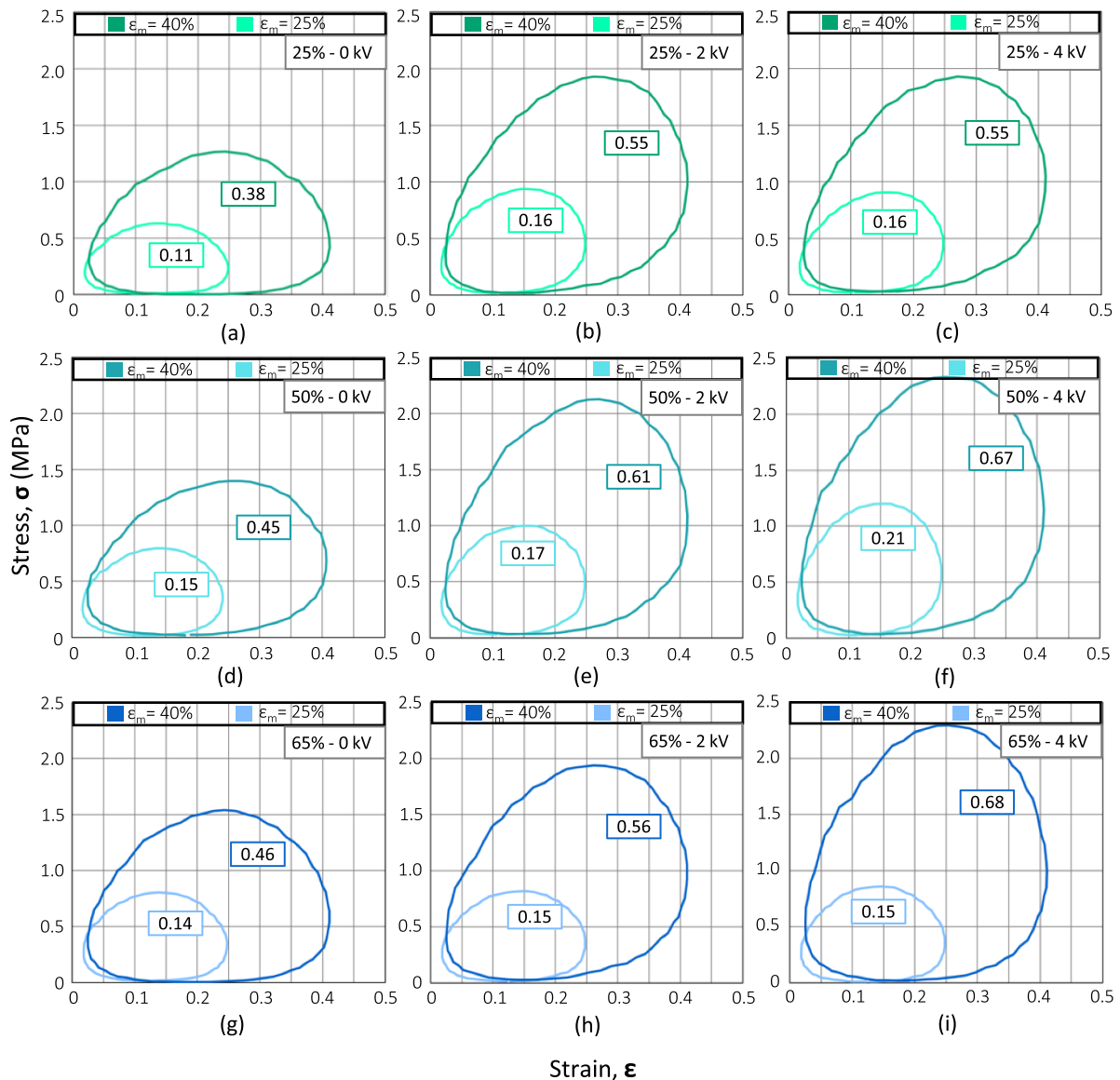


**Figure 7.** Stress–strain curve of the cyclic compression test: first, second, and third row refer to 25%, 50%, and 65% of ceramic powder composition, respectively. Left, middle, and right column refer to 0, 2 and 4 kV polarization voltage, respectively. Labels refer to specific energy dissipated in  $\text{mJ mm}^{-3}$ . The letter at the bottom of each plot refers to the correspondent configuration.

are the possible reasons. First, it is reasonable to assume that a specific strain threshold exists for each configuration: above that threshold the material exhibits a sudden increase on the output voltage signal. This strain threshold clearly depends on the configuration and increases with powder concentrations and polarization voltages, since as observed in figure 4, the higher polarization voltage improves particle alignment. Based on this consideration, the configurations in the third column (4 kV polarization) and, specifically, figure 6(i), would be below their peculiar strain threshold. Second, according to previous researches [59–61], high polarization voltage specimens show optimum responses at higher frequency excitations if compared to lower polarization voltage specimens. Thus, the low output voltage of the configurations in figures 6(c), (f) and (i) may be imputed to an excessively low strain rate. As final

remark, we underline that the increase in powder concentration makes more difficult the fabrication process, specifically with regard to mixture preparation, lower bonding strength of the silicon, and a weaker curing process.

With the same layout of figures 6 and 7 presents the stress–strain curves of a cyclic compression test for each of the nine configurations investigated. Each plot shows two signals, each corresponding to a specific level of maximum strain. The specific energy dissipated by the specimen during the cycle is reported on the top left of each plot in  $\text{mJ mm}^{-3}$ .

All the plots in figure 7 highlight a very high hysteresis, mainly due to the test conditions, which leads to a considerable amount of dissipated energy. Consistent differences are present between the configurations: stronger stress levels, and consequently hysteresis effects, occur at higher

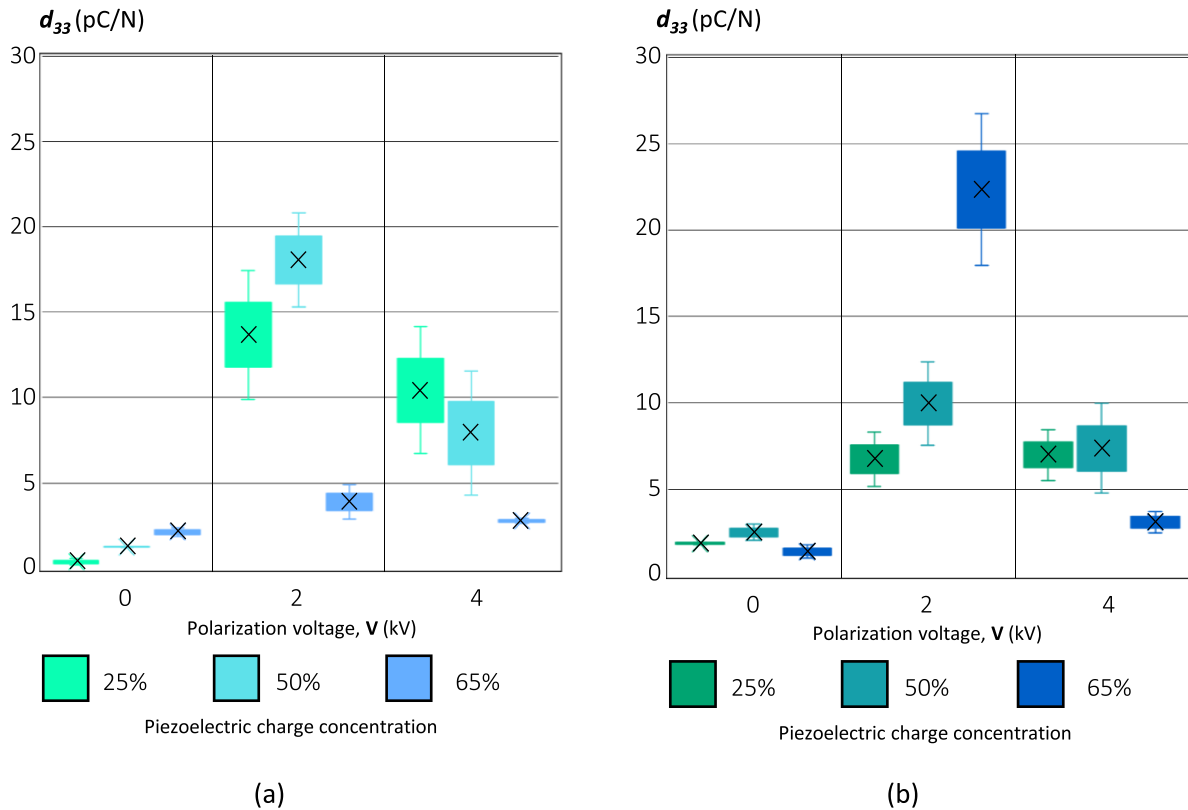


**Figure 8.** Box and whisker charts showing the  $d_{33}$  piezoelectric coefficient and relative experimental error for each configuration investigated considering a maximum strain level of 25% (a) and 40% (b) respectively.

powder concentrations and higher voltage polarization. In addition, higher powder concentration (from first to last row in figure 7) reduces the elastomer volume thus making the specimen harder. Moreover, a stronger polarization (from left to right column in figure 7) increases the stress reached at equal strain level. Also, the Young's modulus exhibits an increment as polarization increases, which can be attributed to the stronger electrostatic repulsion of the piezoelectric particles. As the polarizing electric field intensity increases, a better BaTiO<sub>3</sub> dipoles alignment occurs, as shown by SEM images in figure 4. Mechanically, it leads to a higher sample stiffness and hardness as reported in figure 3, section 2.4.

Figure 7 also remarks the very high compressibility and stretchability of the material, which withstands at high strains without breaking. As already seen in section 2, the piezoe elastomer becomes harder and stiffer as voltage polarization and powder concentration increase. Increasing powder concentration directly changes the mixture composition reducing the amount of rubber, while increasing the voltage polarization acts improving the orientation of particles, since they follow the electric field lines more rigorously.

Figure 8 compares the piezoelectric coefficient  $d_{33}$  of each of the nine configurations investigated with  $\varepsilon_m$  (maximum strain level) equal to 25% (figure 8(a)) and 40% (figure 8(b)), respectively.

The bar charts highlight that the piezoelectric effect consistently changes as a function of the strain levels investigated: specifically, with exception of a specimen, the higher

responses appear for the 40% strain at powder concentration of 25% and 50% and a non-zero polarization voltage. The experimental error is obtained evaluating maximum positive and negative output voltage peaks of the experiments. The piezoelectric coefficients  $d_{33}$  shows a noticeable non-linearity, with some maxima at different levels of strain depending on the configuration chosen. This confirms the existence of an optimum formulation for the piezoe elastomer, which depends on the strain level and the powder concentration.

The unpolarized configurations show in both compression tests a low but non-zero  $d_{33}$  coefficient, even though particles are not aligned. The unpolarized BaTiO<sub>3</sub> powder here used, might perform very slight piezoelectric responses, probably insufficient to justify these results. It comes that the measured value can be attributed to contact electrification, such as friction, contact separations and triboelectric effect, that typically occurs in polymers, particularly in the softest ones as Sutka sustains [62].

Overall, the 2 kV polarized specimens show the highest performances in terms of  $d_{33}$  coefficient in both the compression tests. Counterintuitively, the 4 kV polarization samples present much lower coefficients. This reduction effect has two main contributions: the first is about the reduction of intensity of the electric signal reported in figure 6 and already discussed, whereas the second contribution is given by the increased hardness and stiffness of the correspondent samples.

Moreover, figure 8(b) shows a greater reduction effect of  $d_{33}$  coefficient for the 4 kV poled specimens in the 40%



**Table 1.** Comparison between the piezoelectric coefficient,  $d_{33}$  of most common piezoelectric materials proposed in the literature and the present study.

Denomination	Classification	$d_{33}$ coefficient (pC N <sup>-1</sup> )	Ambient temperature Young's modulus, $E$ (MPa)	Reference
Unpoled $\beta$ -phase PVDF	Plastic	2.5	1500–1800	[63, 64]
Poled $\beta$ -phase PVDF	Plastic	14	1500–1800	[63, 64]
Unpoled $\beta$ -phase PVDF-TrFE	Plastic	2.5	1500–1800	[64–66]
Poled $\beta$ -phase PVDF-TrFE	Plastic	2.5–34	1500–1800	[64–66]
BaTiO <sub>3</sub>	Ceramic	190	160 000–200 000	[19, 67, 68]
PZT	Ceramic	71–593	150 000–230 000	[19, 67, 69]
PbTiO <sub>3</sub>	Ceramic	56	60 000–105 000	[19, 67, 70]
Polyacrylonitrile	Elastomer	40	0.16	[48]
Thermosetting silicone + PZT	Elastomer	60	100	[47]
PVDF-PDMS	Elastomer	8	2–10	[38]
Silicone-based + BaTiO <sub>3</sub> piezoelectric elastomer	Elastomer	3–22	6–12	Present study

strain level than the reduction effect in figure 8(a) for the 25% strain level. This may be attributed to the strong non-linearity of the electric signal intensity over the applied strain already discussed in figure 6, that also affects the  $d_{33}$  parameter. Specifically, it seems that the threshold of strain, raised in the discussion of figure 6, has not been reached in the 4 kV polarized specimens even at 40% of compression, whereas it seems to happen in the 2 kV poled specimens at the same level of strain, thus giving a lower  $d_{33}$  coefficient for the 4 kV poled specimens.

Despite of the low voltage polarization applied, this piezopolymer shows a  $d_{33}$  piezoelectric coefficient higher than classical not brittle materials, like unpoled and poled  $\beta$ -phase PVDF and comparable with poled  $\beta$ -phase PVDF-TrFE. In addition, the proposed material features a remarkably low elastic modulus, compared to typical piezopolymers, in a ratio of about 1 over 1000. Table 1 provides a detailed comparison of the proposed piezoelectric elastomer, other bulky piezoelectric elastomers present in literature and the most common piezoelectric materials in terms of  $d_{33}$  piezoelectric coefficient and Young's modulus. Among other bulky soft piezopolymers, the proposed piezopolymer takes place in between the extremely soft configuration proposed by Fu *et al* [48] and the harder by Mamada *et al* [47], similarly to the one presented by Hu *et al* [38].

Considering its peculiar high hysteresis (see figure 7), a possible application of the proposed piezoelectric silicone-based rubber could be as a smart vibration damper which incorporates sensing functionalities for condition monitoring applications.

## 5. Conclusions

This work reports the study, development, and validation of a soft piezo-polymer with enhanced piezo-elastic response and easy castable in a free shape. Specifically, the work identified a new formulation for soft piezopolymers based on ambient temperature polymerizable silicone rubber mixed with BaTiO<sub>3</sub> ceramic powder, castable in 3D printed plastic moulds.

Through a full factorial test plan, we experimentally investigated the effect of powder concentration and voltage polarization over three levels. For each of the nine configurations investigated, a thin cylindrical specimen was casted, cured and polarized in an ad-hoc designed mould. To evaluate their mechanical and piezoelectric response, we performed cyclic compression tests at two maximum strain levels, registering both their force–displacement characteristic and the output voltage through a specific electrical circuit. The results allowed to identify the optimum configurations in terms of piezoelectric coefficient  $d_{33}$ .


It worth noting that piezoelectric performances of the proposed piezopolymer are higher than other not brittle materials and comparable with  $\beta$ -phase structure PVDF. Among other soft piezopolymers, it claims an intermediate configuration in terms of stiffness and an easier manufacturing method with accessible materials. In addition, this piezopolymer stands out for its extremely stretchable response and its low hardness ensuring large strains without any damage. These characteristics make this piezopolymer particularly suitable for sensors or transducers in multiple application fields, such as health conditions monitoring, mechanical applications, sport wear and equipment, soft robotics, and human motion sensing applications.

## Data availability statement

All data that support the findings of this study are included within the article (and any supplementary files).

## ORCID iDs

Lorenzo Nicolini  <https://orcid.org/0000-0001-6560-8330>

Andrea Sorrentino  <https://orcid.org/0000-0002-7145-5219>

Davide Castagnetti  <https://orcid.org/0000-0003-3300-5716>

## References

- [1] Tadigadapa S and Mateti K 2009 Piezoelectric MEMS sensors: state-of-the-art and perspectives *Meas. Sci. Technol.* **20** 092001
- [2] Gautschi G 2002 'Piezoelectric Sensors,' in *Piezoelectric Sensorics: Force Strain Pressure Acceleration and Acoustic Emission Sensors Materials and Amplifiers* ed G Gautschi (Springer Berlin Heidelberg) pp 73–91
- [3] Varanis M, Silva A, Mereles A and Pederiva R 2018 MEMS accelerometers for mechanical vibrations analysis: a comprehensive review with applications *J. Braz. Soc. Mech. Sci. Eng.* **40** 527
- [4] Curry E J et al 2018 Biodegradable piezoelectric force sensor *Proc. Natl Acad. Sci.* **115** 909–14
- [5] Castagnetti D 2012 Experimental modal analysis of fractal-inspired multi-frequency structures for piezoelectric energy converters *Smart Mater. Struct.* **21** 094009
- [6] Castagnetti D 2011 Fractal-inspired multifrequency structures for piezoelectric harvesting of ambient kinetic energy *J. Mech. Des.* **133** 111005
- [7] Castagnetti D and Radi E 2018 A piezoelectric based energy harvester with dynamic magnification: modelling, design and experimental assessment *Meccanica* **53** 2725–42
- [8] Lu Z-Q, Chen J, Ding H and Chen L-Q 2020 Two-span piezoelectric beam energy harvesting *Int. J. Mech. Sci.* **175** 105532
- [9] Rafique S 2018 *Piezoelectric Vibration Energy Harvesting* (Springer International Publishing) (<https://doi.org/10.1007/978-3-319-69442-9>)
- [10] Blystad L-C J, Halvorsen E and Husa S 2010 Piezoelectric MEMS energy harvesting systems driven by harmonic and random vibrations *IEEE Trans. Ultrason. Ferroelectr. Freq. Control* **57** 908–19
- [11] Mathew A T, Liu C, Ng T Y N and Koh S J A 2019 A high energy dielectric-elastomer-amplified piezoelectric (DEAmP) to harvest low frequency motions *Sens. Actuators A* **294** 61–72
- [12] Murali P, Polcawich R G and Trolier-mckinstry S 2009 Piezoelectric thin films for sensors, actuators, and energy harvesting *MRS Bull.* **34** 658–64
- [13] Safaei M, Sodano H A and Anton S R 2019 A review of energy harvesting using piezoelectric materials: state-of-the-art a decade later (2008–2018) *Smart Mater. Struct.* **28** 113001
- [14] Mohith S, Upadhyaya A R, Navin K P, Kulkarni S M and Rao M 2021 Recent trends in piezoelectric actuators for precision motion and their applications: a review *Smart Mater. Struct.* **30** 013002
- [15] Gao X, Yang J, Wu J, Xin X, Li Z, Yuan X, Shen X and Dong S 2020 Piezoelectric actuators and motors: materials, designs, and applications *Adv. Mater. Technol.* **5** 1900716
- [16] Wang Y, Deng J, Zhang S, Li H, Chen W and Liu Y 2022 Design of a linear-rotary ultrasonic motor for optical focusing inspired by the bionic motion principles of the earthworms *Int. J. Smart Nano Mater.* **13** 346–65
- [17] Wang Y, Deng J, Li H, Tian X, Chen W and Liu Y 2023 A resonant-type thin plate piezoelectric actuator inspired by Koala's locomotion *IEEE Trans. Ind. Electron.* **70** 8235–43
- [18] Ramadan K S, Sameoto D and Evoy S 2014 A review of piezoelectric polymers as functional materials for electromechanical transducers *Smart Mater. Struct.* **23** 033001
- [19] Tressler J F, Alkoy S and Newnham R E 1998 Piezoelectric sensors and sensor materials *J. Electroceram.* **2** 257–72
- [20] Mokhtari F, Azimi B, Salehi M, Hashemikia S and Danti S 2021 Recent advances of polymer-based piezoelectric composites for biomedical applications *J. Mech. Behav. Biomed. Mater.* **122** 104669
- [21] Chen Q X and Payne P A 1995 Industrial applications of piezoelectric polymer transducers *Meas. Sci. Technol.* **6** 249–67
- [22] Mishra S, Unnikrishnan L, Nayak S K and Mohanty S 2019 Advances in piezoelectric polymer composites for energy harvesting applications: a systematic review *Macromol. Mater. Eng.* **304** 1800463
- [23] Usher T D, Cousins K R, Zhang R and Ducharme S 2018 The promise of piezoelectric polymers *Polym. Int.* **67** 790–8
- [24] Smith M and Kar-Narayan S 2022 Piezoelectric polymers: theory, challenges and opportunities *Int. Mater. Rev.* **67** 65–88
- [25] Zheng Z et al 2022 Model-based control of planar piezoelectric inchworm soft robot for crawling in constrained environments 2022 *IEEE 5th Int. Conf. on Soft Robotics (RoboSoft)* (IEEE) April 2022 pp 693–8
- [26] Barbosa A S, Tahara L Z and da Silva M M 2023 Motion planning of a fish-like piezoelectric actuated robot using model-based predictive control *J. Vib. Control* **29** 411–27
- [27] Physik Instrumente *Piezoelectric Transducers & Actuators* (available at: [www.physikinstrumente.com/en/products/piezoelectric-transducers-actuators](http://www.physikinstrumente.com/en/products/piezoelectric-transducers-actuators) [www.piceramic.com/en/expertise/piezo-technology/piezoelectric-materials/](http://www.piceramic.com/en/expertise/piezo-technology/piezoelectric-materials/))
- [28] Sappati K K and Bhadra S 2018 Piezoelectric polymer and paper substrates: a review *Sensors* **18** 3605
- [29] Lee H B, Kim Y W, Yoon J, Lee N K and Park S-H 2017 3D customized and flexible tactile sensor using a piezoelectric nanofiber mat and sandwich-molded elastomer sheets *Smart Mater. Struct.* **26** 045032
- [30] Pan M, Yuan C, Pickford T, Tian J, Ellingford C, Zhou N, Bowen C and Wan C 2021 Piezoelectric-driven self-sensing leaf-mimic actuator enabled by integration of a self-healing dielectric elastomer and a piezoelectric composite *Adv. Intell. Syst.* **3** 2000248
- [31] Banno H 1983 Recent developments of piezoelectric ceramic products and composites of synthetic rubber and piezoelectric ceramic particles *Ferroelectrics* **50** 3–12
- [32] Banno H and Saito S 1983 Piezoelectric and dielectric properties of composites of synthetic rubber and PbTiO<sub>3</sub> or PZT *Jpn. J. Appl. Phys.* **22** 67
- [33] Hikita K, Yamada K, Nishioka M and Ono M 1983 Piezoelectric properties of the porous PZT and the porous PZT composite with silicone rubber *Ferroelectrics* **49** 265–72
- [34] Qi Y, Jafferis N T, Lyons K Jr, Lee C M, Ahmad H and McAlpine M C 2010 Piezoelectric ribbons printed onto rubber for flexible energy conversion *Nano Lett.* **10** 524–8
- [35] Tsai J-W, Wang J-J and Su Y-C 2014 Piezoelectric rubber films for autonomous physiological monitoring systems *Sens. Actuators A* **215** 176–83
- [36] Wang J-J, Su H-J, Hsu C-I and Su Y-C 2014 Composite piezoelectric rubber band for energy harvesting from breathing and limb motion *J. Phys. Conf. Ser.* **557** 12022
- [37] Wang J-J, Tsai J-W and Su Y-C 2013 Piezoelectric rubber films for highly sensitive impact measurement *J. Micromech. Microeng.* **23** 75009
- [38] Hu S, Shi Z, Zhao W, Wang L and Yang G 2019 Multifunctional piezoelectric elastomer composites for smart biomedical or wearable electronics *Composites B* **160** 595–604
- [39] Seo J, Hur J, Kim M-S, Lee T-G, Seo S J, Han S H and Seo J-H 2021 All-organic piezoelectric elastomer formed through the optimal cross-linking of semi-crystalline polyrotaxanes *Chem. Eng. J.* **426** 130792
- [40] Cheng X, Gong Y, Liu Y, Wu Z and Hu X 2020 Flexible tactile sensors for dynamic triaxial force measurement based on piezoelectric elastomer *Smart Mater. Struct.* **29** 075007

- [41] Khastgir D and Adachi K 1999 Piezoelectric and dielectric properties of siloxane elastomers filled with bariumtitanate *J. Polym. Sci. B* **37** 3065–70
- [42] Wang X, Liu Q, Hu X, You M, Zhang Q, Hu K, Zhang Q and Xiang Y 2022 Highly stretchable lactate-based piezoelectric elastomer with high current density and fast self-healing behaviors *Nano Energy* **97** 107176
- [43] Chou X et al 2018 All-in-one filler-elastomer-based high-performance stretchable piezoelectric nanogenerator for kinetic energy harvesting and self-powered motion monitoring *Nano Energy* **53** 550–8
- [44] Wang X, Zhang Q, Zhu H, Wu F, Qiao Y, Jia K, Xiang Y and Hu X 2023 A highly efficient piezoelectric elastomer with a green product cycle from fabrication to degradation *J. Mater. Sci.* **58** 4840–52
- [45] Cafarelli A, Losi P, Salgarella A R, Barsotti M C, di Cioccio I B, Foffa I, Vannozzi L, Pingue P, Soldani G and Ricotti L 2019 Small-caliber vascular grafts based on a piezoelectric nanocomposite elastomer: mechanical properties and biocompatibility *J. Mech. Behav. Biomed. Mater.* **97** 138–48
- [46] Liu Y et al 2020 Electronic skin from high-throughput fabrication of intrinsically stretchable lead zirconate titanate elastomer *Research* **2020** 1085417
- [47] Mamada S, Yaguchi N, Hansaka M, Yamato M and Yoshida H 2014 Performance improvement of piezoelectric-rubber by particle formation of linear aggregates *J. Appl. Polym. Sci.* **131** 39862
- [48] Fu R, Tu L, Guan Y, Wang Z, Deng C, Yu P, Tan G, Ning C and Zhou L 2022 Intrinsically piezoelectric elastomer based on crosslinked polyacrylonitrile for soft electronics *Nano Energy* **103** 107784
- [49] Dow Chemical SYLGARD™ 184 Silicone Elastomer (available at: [www.dow.com/documents/en-us/productdatasheet/11/11-31/11-3184-sylgard-184-elastomer.pdf](http://www.dow.com/documents/en-us/productdatasheet/11/11-31/11-3184-sylgard-184-elastomer.pdf))
- [50] PubChem Barium titanate(IV), powder, <3 μm, 99% (available at: <https://pubchem.ncbi.nlm.nih.gov/substance/24852494>)
- [51] Stratasys (available at: [www.stratasys.com/](http://www.stratasys.com/))
- [52] Aim-TTi (available at: [www.aimtti.com/](http://www.aimtti.com/))
- [53] XP Power (available at: [www.xppower.com/](http://www.xppower.com/))
- [54] Mitutoyo Shore Durometer HH-332 Shore A digital/long (available at: [https://shop.mitutoyo.eu/web/mitutoyo/en/mitutoyo/Hardmatic%20HH-300/Shore%20Durometer%20/\\$catalogue/mitutoyoData/PR/811-332-10/index.xhtml](https://shop.mitutoyo.eu/web/mitutoyo/en/mitutoyo/Hardmatic%20HH-300/Shore%20Durometer%20/$catalogue/mitutoyoData/PR/811-332-10/index.xhtml))
- [55] Galdabini (available at: [www.galdabini.it/](http://www.galdabini.it/))
- [56] National Instruments USB-6251 (available at: [www.ni.com/en-ca/support/model.usb-6251.html](http://www.ni.com/en-ca/support/model.usb-6251.html))
- [57] Park C H 2001 On the circuit model of piezoceramics *J. Intell. Mater. Syst. Struct.* **12** 515–22
- [58] Al Ahmad M and Allataifeh A 2018 Electrical extraction of piezoelectric constants *Heliyon* **4** e00910
- [59] Kressmann R 2001 Linear and nonlinear piezoelectric response of charged cellular polypropylene *J. Appl. Phys.* **90** 3489–96
- [60] Qiu Y, Sun S, Xu C, Wang Y, Tian Y, Liu A, Hou X, Chai H, Zhang Z and Wu H 2021 The frequency-response behaviour of flexible piezoelectric devices for detecting the magnitude and loading rate of stimuli *J. Mater. Chem. C* **9** 584–94
- [61] Varga M, Morvan J, Diorio N, Buyuktanir E, Harden J, West J L and Jáklí A 2013 Direct piezoelectric responses of soft composite fiber mats *Appl. Phys. Lett.* **102** 153903
- [62] Šutka A, Sherrell P C, Shepelin N A, Lapčinskis L, Mālnieks K and Ellis A V 2020 Measuring piezoelectric output—fact or friction? *Adv. Mater.* **32** 2002979
- [63] Roopaa T S, Narasimha Murthy H N, Kumar P V and Krishna M 2018 Development and characterization of PVDF thin films for pressure sensors *Mater. Today Proc.* **5** 21082–90
- [64] Oliveira G L, Costa C A, Teixeira S C S and Costa M F 2014 The use of nano- and micro-instrumented indentation tests to evaluate viscoelastic behavior of poly(vinylidene fluoride) (PVDF) *Polym. Test* **34** 10–16
- [65] Hu X, You M, Yi N, Zhang X and Xiang Y 2021 Enhanced piezoelectric coefficient of PVDF-TrFE films via *in situ* polarization *Front. Energy Res.* **9** 621540
- [66] Gomes J, Serrado Nunes J, Sencadas V and Lanceros-Mendez S 2010 Influence of the  $\beta$ -phase content and degree of crystallinity on the piezo- and ferroelectric properties of poly(vinylidene fluoride) *Smart Mater. Struct.* **19** 065010
- [67] Abbasipour M, Khajavi R and Akbarzadeh A H 2022 A comprehensive review on piezoelectric polymeric and ceramic nanogenerators *Adv. Eng. Mater.* **24** 2101312
- [68] Cordero F 2018 Quantitative evaluation of the piezoelectric response of unpoled ferroelectric ceramics from elastic and dielectric measurements: tetragonal BaTiO<sub>3</sub> *J. Appl. Phys.* **123** 094103
- [69] Li Y, Feng S, Wu W and Li F 2015 Temperature dependent mechanical property of PZT film: an investigation by nanoindentation *PLoS One* **10** e0116478
- [70] Kalinichev A G, Bass J D, Sun B N and Payne D A 1997 Elastic properties of tetragonal PbTiO<sub>3</sub> single crystals by Brillouin scattering *J. Mater. Res.* **12** 2623–7